

RoboSubtaskNet: Temporal Sub-task Segmentation for Human-to-Robot Skill Transfer in Real-World Environments

Dharmendra Sharma, Archit Sharma, John Reberio, Vaibhav Kesharwani, Peeyush Thakur, Narendra Kumar Dhar, and Laxmidhar Behera

Abstract— Temporally locating and classifying fine-grained sub-task segments in long, untrimmed videos is crucial to safe human–robot collaboration. Unlike generic activity recognition, collaborative manipulation requires sub-task labels that are directly *robot-executable*. We present RoboSubtaskNet, a multi-stage human-to-robot sub-task segmentation framework that couples attention-enhanced 3D features (RGB+optical flow) with a modified MS-TCN employing a Fibonacci dilation schedule to capture better short-horizon transitions such as reach–pick–place. The network is trained with a composite objective comprising cross-entropy and temporal regularizers (truncated MSE and a transition-aware term) to reduce over-segmentation and to encourage valid sub-task progressions. To close the gap between vision benchmarks and control, we introduce RoboSubtask, a dataset of healthcare and industrial demonstrations annotated at the sub-task level and designed for deterministic mapping to manipulator primitives. Empirically, RoboSubtaskNet outperforms MS-TCN and MS-TCN++ on GTEA and our RoboSubtask benchmark (boundary-sensitive and sequence metrics), while remaining competitive on the long-horizon Breakfast benchmark. Specifically, RoboSubtaskNet attains $F1@50 = 79.5\%$, $Edit = 88.6\%$, $Acc = 78.9\%$ on GTEA; $F1@50 = 30.4\%$, $Edit = 52.0\%$, $Acc = 53.5\%$ on Breakfast; and $F1@50 = 94.2\%$, $Edit = 95.6\%$, $Acc = 92.2\%$ on RoboSubtask. We further validate the full perception-to-execution pipeline on a 7-DoF Kinova Gen3 manipulator, achieving reliable end-to-end behavior in physical trials (overall task success approx 91.25%). These results demonstrate a practical path from sub-task level video understanding to deployed robotic manipulation in real-world settings.

Index Terms— sub-task learning, imitation learning, video classification, robot manipulator, and learning from demonstration.

I. INTRODUCTION

Deployment of robots in real-world scenarios, particularly in healthcare [1] and industrial [2] settings, is no longer limited to repetitive or isolated automation tasks. Instead, robots are increasingly expected to operate collaboratively alongside humans, facilitating complex workflows that include interactive tasks such as handovers, pick and place operations, pouring liquids into containers, and cleaning work surfaces. These collaborative settings demand precision, reliability, and adaptability to human actions and environmental variability, making the design of robust perception and execution frameworks a critical requirement. Unlike full human activity recognition (HAR), these domains require decomposition of complex demonstrations into *fine-grained robot-executable sub-tasks*. Bridging human video demonstrations with reliable robotic execution requires (i) *robust spatiotemporal perception*, (ii) *precise temporal segmentation into primitives*, and (iii) a *deterministic mapping*

from predicted sub-task labels to robot skills.

Research on human–robot collaboration has led to different approaches that improve interaction schemes and execution efficiency. Han *et al.* [3] and Hawkins *et al.* [4] employed probabilistic graphical models to estimate task progress by jointly tracking hand and object positions. Brooks *et al.* [5] developed proactive robot assistants with multimodal recognition, while Fishman *et al.* [6] introduced collaborative interaction models that improved the efficiency of human–robot learning. Johns *et al.* [7] proposed coarse-to-fine imitation learning, enabling robots to perform manipulation tasks from a single demonstration. Similarly, Semeraro *et al.* [8] surveyed the integration of machine learning in collaborative robotics, and Thumm *et al.* [9] introduced the “Human–Robot Gym” to benchmark reinforcement learning algorithms from demonstrations.

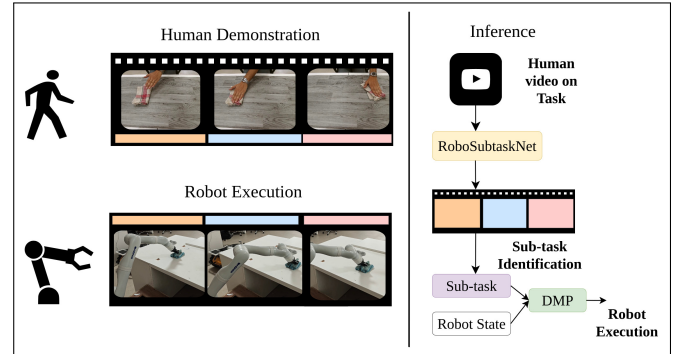


Fig. 1: RoboSubtaskNet pipeline for Human-to-Robot skill transfer.

Despite these advances, segmenting full task human videos into *robot-executable sub-tasks* remains a challenge. Vision-based HAR datasets such as GTEA or EGTEA [10], Breakfast [11], and 50Salads [12] provide valuable benchmarks for activity parsing but are not aligned with robotic execution needs. Their annotations focus on high-level semantic activities (e.g., “make tea”), while manipulator control requires primitive-level instructions such as *reach*, *pick*, or *place*. As existing HAR datasets are mismatched for manipulator-level execution, we create *RoboSubtask*, which contains human demonstrations with sub-task level labels explicitly designed for robot mapping. To ensure alignment with robotic control, our dataset defines sub-tasks that are directly mappable to manipulator primitives, as summarized in Table I. Temporal action segmentation methods have made notable progress

TABLE I: Definition of some fundamental sub-tasks

Sub-task	Definition
Reach	Moving the hand or end-effector towards an object
Pick	Lifting an object at a certain height
Place	Positioning a picked object at a target location
Retract	Returning to home position
Pour	Pouring contents from one object into another
Wipe	Cleaning the work surface
Move	Movement of the hand with objects

in parsing long and untrimmed videos. MS-TCN [13] and MS-TCN++ [14] introduced dilated temporal convolutions and stage-wise refinement to improve segmentation quality, while Yi *et al.* [15] and Ding *et al.* [16] further enhanced temporal modeling using self-attention and boundary-aware mechanisms. However, these models are primarily evaluated on video classification benchmarks rather than robotic execution pipelines. They are also more computationally expensive than TCNs, and their dilation schedules are optimized for long-horizon activities such as cooking, rather than the short-horizon sub-tasks required in manipulation.

To overcome these gaps, we propose a novel framework, *human-to-robot sub-task segmentation*, that integrates I3D-based spatiotemporal feature extraction [17] with a modified MS-TCN for fine-grained segmentation on manipulators.

The key **contributions** of this work are as follows:

- A feature-enhanced I3D backbone is designed by appending an attention fusion layer, enabling more discriminative spatio-temporal representations and reliable recognition of subtle human motions.
- A fibonacci-dilated MS-TCN is proposed, which effectively models short-horizon transitions (e.g., reach-pick-place) in manipulation tasks compared to conventional dilation schedules.
- A new dataset, RoboSubtask, is introduced, comprising healthcare and industrial demonstrations annotated at the sub-task level and directly mappable to manipulator primitives.

The framework is validated through experiments on a Kinova Gen3 manipulator, demonstrating end-to-end execution from human video input to sequential primitive control.

The workflow of the proposed framework is shown in Figure 1. Our focus is on short-horizon manipulation sub-tasks in healthcare and industrial settings; extension to more complex long-horizon activities is left for future work.

The rest of the paper is organized as follows: Section II presents the proposed methodology, Section III discusses the experimental results, and Section IV concludes the paper.

II. PROPOSED METHODOLOGY

The proposed methodology comprises four phases: (a) *dataset creation*, (b) *feature extraction and modality fusion*, (c) *sub-task learning*, and (d) *robot execution model*.

A. Dataset creation

We consider a dataset of T manipulation tasks $\mathcal{T} = \{t_1, \dots, t_T\}$ recorded with an RGB vision sensor mounted

on the robot. For each task $t \in \mathcal{T}$, we acquire N_t labeled videos. Each video is temporally annotated at the *frame* level manually with labels of a sub-task from vocabulary V (a task to sub-task sequence summarized in Table II); annotations are stored per video as a temporal label sequence for flexible downstream processing. We create a hold-out split by reserving a fraction r_{val} of videos per task for validation and testing, leaving $(1 - r_{\text{val}})N_t$ for training. Let $A = \{a_1, \dots, a_{|A|}\}$ denote a set of augmentations that preserve appearance and geometry applied independently to each training video; the effective multiplier of augmentations is $(1 + |A|)$. The per-task and total training sizes are therefore $N_t^{\text{train,aug}} = (1 - r_{\text{val}})N_t(1 + |A|)$, $N^{\text{train,aug}} = \sum_{t \in \mathcal{T}} N_t^{\text{train,aug}}$, and the holdout size per task is $N_t^{\text{val}} = r_{\text{val}}N_t$. Data collection spans multiple users, objects, and environments to promote generalization before feature extraction.

TABLE II: Task to sub-task mapping used for annotation and control on RoboSubtask (Columns indicate sub-task vocabulary. ✓ denotes sub-tasks in each task’s sequence.)

Task	Reach	Pick	Move	Pour	Move	Give	Place	Wipe	Retract
Pick & Place	✓	✓	✓				✓		✓
Pick & Pour	✓	✓	✓	✓	✓		✓		✓
Cleaning	✓							✓	
Pick & Give	✓	✓					✓		✓

B. Feature extraction and modality fusion

a) *I3D for video features*: Action segmentation requires representations that capture appearance and motion. Inflated 3D ConvNets (I3D) [18] learn spatiotemporal features directly from short clips, going beyond framewise 2D CNNs by modeling temporal evolution. Pre-training on a large video kinetics dataset [19] makes I3D an effective standard feature encoder for human demonstrations with limited task-specific labels. In addition, downstream temporal models such as TCN and MSTCN operate on compact, high-level descriptors rather than raw pixels; I3D supplies precisely these per-time-step embeddings, improving segmentation robustness and data efficiency.

b) *Raw video to feature matrices*.: Let a demonstration video contain F RGB frames. We derive two frame sequences (shown in Figure 2a)

$$\{F_i^{\text{rgb}}\}_{i=1}^F \quad \text{and} \quad \{F_i^{\text{flow}}\}_{i=1}^F,$$

where F_i^{flow} denotes the optical-flow representation between frames i and $i+1$. Passing each sequence through I3D heads yields D (say 1024) descriptors per time step as

$$\mathbf{f}_t^{\text{rgb}} = \phi_{\text{I3D}}^{\text{rgb}}(F_t^{\text{rgb}}) \in \mathbb{R}^D \quad \text{and} \quad \mathbf{f}_t^{\text{flow}} = \phi_{\text{I3D}}^{\text{flow}}(F_t^{\text{flow}}) \in \mathbb{R}^D,$$

for $t = 1, \dots, T$. I3D includes temporal down-sampling (strided 3D convolutions and pooling) and $T \approx \lceil F/s \rceil$ with temporal stride $s \approx 8$. For efficient and archival reuse, we store

$$\mathbf{X}^{\text{rgb}} = [\mathbf{f}_1^{\text{rgb}}, \dots, \mathbf{f}_T^{\text{rgb}}]^\top \in \mathbb{R}^{T \times D} \quad \text{and}$$

$$\mathbf{X}^{\text{flow}} = [\mathbf{f}_1^{\text{flow}}, \dots, \mathbf{f}_T^{\text{flow}}]^\top \in \mathbb{R}^{T \times D}$$

for downstream training.

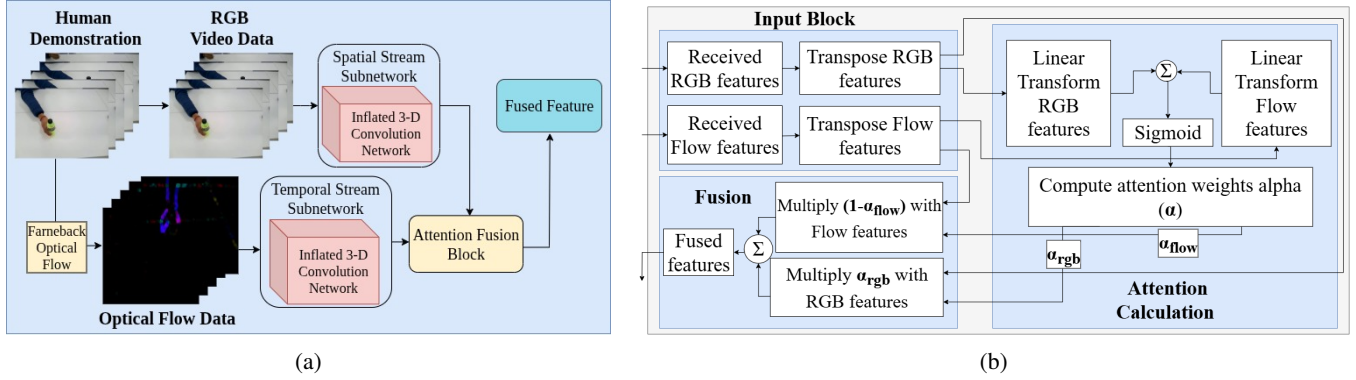


Fig. 2: Feature extraction and attention-fusion module. (a) I3D-based feature extractor, (b) Attention fusion schematic.

c) *Attention-based fusion of RGB and Flow features*: Once we have extracted the RGB features f_t^{rgb} and flow features f_t^{flow} from the I3D model, the next challenge is to combine them effectively. A straightforward approach would be to concatenate them into a single $D + D$ -dimensional feature vector per frame. However, such fixed fusion treats both modalities as equally important at all times, which is often not true in practice.

For instance, when the hand is in motion, optical flow may carry more meaningful cues, whereas during precise object interactions (like grasping), RGB appearance becomes more critical. To address this imbalance, we introduce an attention-based fusion mechanism shown in Figure 2b that allows the model to adaptively assign importance to each modality for every frame and every dimension of the feature. It uses a small neural network that takes RGB and flow as input and predicts attention weights for each frame. Formally, for each frame t , a fully connected shallow layer computes an attention coefficient $\alpha(t) \in [0, 1]^D$ as

$$\alpha(t) = \sigma(W_a \cdot [f_t^{rgb}; f_t^{flow}] + b_a), \quad (1)$$

where W_a and b_a are learnable parameters and $\sigma(\cdot)$ denotes sigmoid activation. The fused feature is computed as

$$f_t^{fused} = \alpha(t) \odot f_t^{rgb} + (1 - \alpha(t)) \odot f_t^{flow}. \quad (2)$$

Here, \odot denotes element-wise multiplication. Intuitively, if $\alpha(t) \approx 1$, the model is based on RGB whereas for $\alpha(t) \approx 0$, the model focuses on flow. In most cases, $\alpha(t)$ learns nuanced combinations, capturing both appearance and motion cues.

The network design allows for dynamic emphasis on the most informative modality depending on the sub-task. For example, *reach* and *move* are dominated by motion cues (flow), while *pick* or *place* often require visual detail (RGB). Table III illustrates typical dominant features in different sub-tasks.

Compared to concatenation or simple averaging, attention fusion provides several advantages. With adaptive weighting, it learns the relative importance of RGB and flow. The weighting changes across time and sub-tasks, making the representation more robust. The dimension of the fused representation is D instead of $2D$, thus reducing computational

TABLE III: Dominant feature modality across sub-tasks

Sub-task	Likely dominant feature
Reach	Flow (motion of hand)
Pick	RGB (appearance of fingers around object)
Place	RGB (object shape on surface)
Retract	Flow (hand moving away)
Pour	RGB
Wipe	Flow
Move	Flow

cost. By focusing on the right modality at the right time, the model achieves better temporal consistency and accuracy in sub-task recognition. Therefore, attention-based fusion allows the system to intelligently decide “which modality matters more” at each step of the task, resulting in stronger and more interpretable feature embeddings for downstream segmentation. Following feature extraction from the I3D model with an attention fusion block, the fused features are fed into the sub-task segmentation network. In contrast to the exponential dilation schedule used in MS-TCN (i.e., $d_l = 2^{l-1}$), we employ a Fibonacci dilation scheme that is better suited to short-horizon manipulation transitions.

C. Sub-task learning

Understanding complex human activities requires modeling long-range temporal structure beyond the per-frame features. While attention-enhanced I3D (RGB+Flow) provides rich local spatiotemporal descriptors, human demonstrations are inherently sequential, consisting of interdependent sub-tasks (e.g., *reach*, *pick*, *pour*, *place*, *retract*). We, therefore, adopt a multistage temporal convolutional architecture that captures long-range dependencies and progressively refines boundaries. Our contributions are twofold: (i) a *Fibonacci-based dilation schedule* and (ii) a *transition-aware loss* that discourages invalid label switches.

Here, $\mathbf{X} \in \mathbb{R}^{T \times D}$ denotes the fused feature sequence with T time steps and D channels. A stage applies L dilated layers with kernel size k and dilation factors $\{d_l\}_{l=1}^L$. We denote the hidden sequence after layer l as $H^{(l)} \in \mathbb{R}^{T \times D}$ (with $\mathbf{H}^{(0)} = \mathbf{X}$).

1) *Single stage TCN*: Each layer is a dilated 1D temporal convolution with a residual connection:

$$H_t^{(l)} = \text{ReLU}((W^{(l)} *_{d_l} H_t^{(l-1)}) + b^{(l)}) + H_t^{(l-1)}, \quad (3)$$

where $*_{d_l}$ denotes convolution along time with dilation d_l , $W^{(l)} \in \mathbb{R}^{D \times D \times k}$ are the layer weights, and $b^{(l)} \in \mathbb{R}^D$ is a bias. With $k=3$, each layer expands the receptive field (RF) by $k-1=2$ time steps.

a) *Fibonacci dilated convolutions*: Conventional temporal segmentation models employ exponentially increasing dilation factors such as $d_l=2^{l-1}$ (e.g., 1, 2, 4, 8, ...). It also creates a sparse sampling pattern, skipping over important intermediate frames and causing the model to miss subtle transitions. To overcome this, we introduce a Fibonacci dilation strategy.

$$d_l = F_{l+1}, \quad l = 1, \dots, L, \quad (4)$$

where F_{l+1} are Fibonacci numbers (1, 1, 2, 3, 5, ...). With k kernel as 3, the receptive field after L layers is

$$\text{RF} = 1 + (k-1) \sum_{l=1}^L F_{l+1} = 1 + 2(F_{L+3} - 2), \quad (5)$$

yielding denser temporal coverage of short-horizon events while still expanding context for move-like segments. An illustrative residual layer is shown in Figure 3.

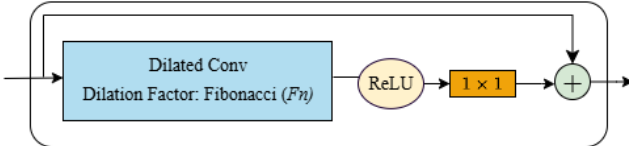


Fig. 3: Dilated residual layer with Fibonacci dilation factors.

2) *Frame wise classification*: A 1×1 temporal convolution maps $H_t^{(L)}$ to class logits, and a softmax yields per-frame probabilities:

$$P_t = \text{Softmax}(W_o H_t^{(L)} + b_o), \quad W_o \in \mathbb{R}^{C \times D}, b_o \in \mathbb{R}^C, \quad (6)$$

where C is the number of sub-task classes and $P_t \in \mathbb{R}^C$ is on the probability simplex.

3) *Multi-stage refinement*: We stack S stages; stage s refines the predictions of stage $s-1$,

$$Y^{(1)} = F(X), \quad (7)$$

$$Y^{(s)} = F(Y^{(s-1)}), \quad s = 2, \dots, S, \quad (8)$$

where $F(\cdot)$ denotes a single-stage TCN (weights are not shared between stages). This progressively reduces over-segmentation and sharpens boundaries.

4) *Loss Function*: We minimize the combined loss function

$$\mathcal{L} = \sum_{s=1}^S \left(L_{\text{CE}}^{(s)} + \lambda L_{\text{T-MSE}}^{(s)} + \gamma L_{\text{Trans}}^{(s)} \right), \quad (9)$$

with nonnegative weights λ, γ and truncation $\tau > 0$. Some loss functions used in our framework are:

a) *Cross entropy*: For ground-truth labels $c_t \in \{1, \dots, C\}$,

$$L_{\text{CE}}^{(s)} = -\frac{1}{T} \sum_{t=1}^T \log P_t[c_t]. \quad (10)$$

b) *Temporal smoothing (T-MSE)*: To reduce flicker and over-segmentation, we penalize abrupt changes in log-probabilities:

$$L_{\text{T-MSE}}^{(s)} = \frac{1}{T-1} \sum_{t=2}^T \min \left(\|\log P_t - \log P_{t-1}\|_2^2, \tau \right). \quad (11)$$

c) *Transition aware*: Let $M \in \{0, 1\}^{C \times C}$ encode *invalid* transitions ($M_{ij}=1$ if $i \rightarrow j$ is invalid, else 0). Define a transition weight

$$w_t = P_{t-1}^\top M P_t \in [0, 1], \quad (12)$$

modulate the temporal change accordingly;

$$L_{\text{Trans}}^{(s)} = \frac{1}{T-1} \sum_{t=2}^T w_t \|P_t - P_{t-1}\|_1. \quad (13)$$

This discourages rapid switches that imply implausible sub-task progressions while leaving valid transitions less penalized.

D. Robot execution model

The robot execution model key components are discussed below.

1) *Learning trajectory using DMP*: Each sub-task (pick, retract, tilt, etc.) is predefined and trained using a DMP model. The DMP framework allows the creation of a library for these sub-tasks, facilitating smooth and human-like robot manipulator movements. DMP can be learned through demonstration or programmed manually to generate the appropriate trajectories. The DMPs in this work are formulated to generate trajectories in the Cartesian space for the robot's end-effector pose, specifically controlling its x , y , and z coordinates. To describe trajectory evolution, the DMP equation is represented as

$$\tau \ddot{x} = \alpha(\beta(g - x) - \tau \dot{x}) + f(x), \quad (14)$$

where τ is the temporal scaling factor that adjusts the duration of the movement. x , \dot{x} , and \ddot{x} represent position, velocity, and acceleration, respectively. g is the target position, with α controlling the speed of convergence to the target. β controls the spring-like behavior of the trajectory, shaping the movement, and $f(x)$ is the forcing function that further refines the trajectory. The forcing function is represented as

$$f(s) = \frac{\sum_{i=1}^N w_i \psi_i(s)}{\sum_{i=1}^N \psi_i(s)}, \quad \psi_i(s) = \exp \left(-\frac{(s - c_i)^2}{2\sigma^2} \right), \quad \tau_c s' = -\alpha_x s,$$

where w_i are weights, $\psi_i(s)$ is a basis function, τ_c is the temporal scaling factor, s is the phase variable, and α_x is a time constant. The detailed DMP trajectory learning is taken from [20].

2) *Object detection*: The vision-based grasping process begins with object detection. The robot captures an RGB image of the workspace and processes it through a YOLOv8-n model, which has been trained on custom objects (*bottle*, *cup*, *bowl*, *medicine syrup*, *mop*, *box*) targeted for manipulation. Upon a successful detection, a bounding box is drawn around the object. The center pixel coordinates (u, v) of this

bounding box are calculated. These 2D image coordinates are then combined with data from a depth sensor, which provides a corresponding per-pixel distance map. Indexing this depth map at the location (u, v) yields the distance d from the camera to the object.

3) *Visual Servoing with a Proportional Controller*: A proportional (P) controller is used to drive the end-effector from its current position to the target position. The components of this approach are control law design and implementation system constraints.

a) *Control objective*: The main goal is to control the robotic arm's position in Cartesian coordinates (x, y, z) by minimizing position errors through velocity adjustments. A P-controller determines the difference between the desired and current positions, generating proportional velocity commands for the arm.

b) *Proportional gains*: To ensure proper sensitivity of the controller, proportional gains k_x and k_{pz} are considered. k_x is used to control the arm's forward and backward movements in x -axis, while k_{pz} regulates movements in y and z directions.

c) *Constraints*: To prevent too fast movement, velocity constraints are applied on all axes. When position errors are within defined thresholds, velocities are set to zero, allowing the arm to stabilize without unnecessary movements.

d) *Control laws*: The P-controller generates velocity commands proportional to position errors. For the x -axis (depth): $v_x = k_x(d - d_{ref})$, where d is the measured depth and $d_{ref} = 0.5$ m. For the y and z axes: $v_y = k_{pz}e_y$ and $v_z = k_{pz}e_z$, where e_y and e_z are the position errors in y and z , respectively. Velocity commands are saturated to respect axis limits and are set to zero when errors lie within the tolerance band.

4) *Coordinate Transformation and Task Execution via DMP*: The proportional controller continues until the positional error is minimized and the velocities for all axes converge to zero, indicating the end-effector is aligned with the target. Once the P-controller has achieved alignment, the final 3D coordinate of the object is transformed into the robot base frame using the ROS TF2 library to find the static transform between the camera and base frames. This transformed coordinate is passed as the goal g to the DMP corresponding to the desired sub-task. DMP then generates a smooth trajectory from the current end-effector position to the target for final movement.

III. EXPERIMENTS AND RESULTS

We evaluated the proposed perception-to-execution pipeline on public temporal segmentation benchmarks and on our robotic platform with RoboSubtask, assessing both vision metrics and end-to-end task execution.

A. Experimental setup

The experimental setup consists of the following.

1) *Hardware*: A Kinova Gen3 (7-DOF) robot manipulator executes the predicted sub-task sequence. An Intel RealSense depth camera (D410) is rigidly mounted on the arm for RGB-depth capture. Model training/inference is performed on a single NVIDIA GTX 1650 (4GB VRAM).

2) *Software*: We use robot operating system (ROS) with Kinova Kortex APIs [21] for low-level control and vision acquisition. Temporal models are implemented in PyTorch.

B. Datasets and metrics used

We evaluate the proposed framework on three challenging datasets: Georgia Tech Egocentric Activities (GTEA) [10], the Breakfast [11], and our RoboSubtask dataset.

1) *RoboSubtask description*: In our experiments, we use $T = 4$ tasks, $\mathcal{T} = \{\text{pick and place, pick and pour, pick and give, cleaning}\}$ recorded with RGB camera. For each task, $N_t = 200$; the holdout fraction is $r_{\text{val}} = 0.20$ (unaltered). The augmentation set is $A = \{\text{horizontal flip, brightness adjustment}\}$ so $|A| = 2$ and the multiplier is $1 + |A| = 3$. Hence, $N_t^{\text{train, aug}} = (1 - 0.20) \times 200 \times 3 = 480$ videos per task, $N^{\text{train, aug}} = 4 \times 480 = 1,920$, and $N_t^{\text{val}} = 0.20 \times 200 = 40$, totaling 160 hold-out videos across tasks. All videos are frame-wise annotated using the sub-task vocabulary in Table II.

Following the MS-TCN metrics [13], [14], we use *frame-wise accuracy*, segmental $F1@ \{10, 25, 50\}$ (IoU thresholds), and *Edit* score to evaluate the performance of various methods in the data sets mentioned above. Accuracy captures per-frame correctness; $F1$ emphasizes boundary quality; *Edit* penalizes over-segmentation and order errors.

C. Training and implementation details

We train a multi-stage temporal model with S stages; each stage comprises L 1D convolutional layers with a dilation schedule d_l , kernel size k , and C channels, using ReLU activations and residual connections. Regularization includes dropout with probability p after temporal convolutions and ℓ_2 weight decay of w_d . Input features are z-score normalized per channel over the training split. To address class imbalance, inverse-frequency weights are applied to the cross-entropy term. The composite loss uses hyperparameters λ , γ , and τ to balance frame-level accuracy, temporal smoothness, and transition stability.

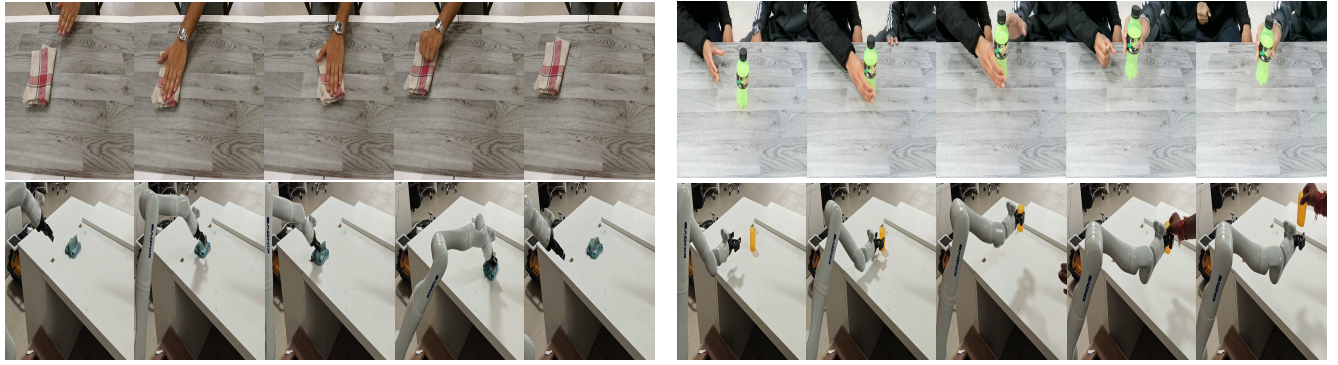
Optimization used AdamW with initial learning rate η_0 , a cosine decay schedule with warmup of E_w epochs, batch size B , gradient clipping at g_{max} , and mixed precision. Training proceeds up to E_{max} epochs with early stopping (patience P) monitoring a validation metric; the checkpoint that maximizes a selection metric ($F1@50$) is reported. At inference, we apply repetition-collapsing and an optional median filter of window W to suppress spurious spikes and improve segment smoothness.

a) *Instantiation for our experiments*: We use $S = 4$ stages with $L = 10$ layers per stage and *Fibonacci* dilated convolutions; kernel $k = 3$, channels $C = 64$, ReLU, residual connections; dropout $p = 0.5$; weight decay $w_d = 1 \times 10^{-4}$. Features are z-score normalized per channel; class imbalance is handled via inverse frequency weights in the cross-entropy term. The loss hyperparameters are $\lambda = 0.15$, $\gamma = 0.25$, $\tau = 4.0$. The models are implemented in PyTorch and trained on a single NVIDIA GTX 1650 (4 GB VRAM) with AdamW at $\eta_0 = 5 \times 10^{-4}$, cosine decay with $E_w = 5$ warm-up epochs,



(a) Pick and place

(b) Pick and pour



(c) Cleaning of a table

(d) Pick and give

Fig. 4: For each task: (a) pick & place, (b) pick & pour, (c) table cleaning, & (d) pick & give. The top images show their human demonstrations, and the bottom images show the corresponding task sequence of the robot (sequence left to right).

batch size $B = 8$, gradient clipping $g_{\max} = 5.0$, and mixed precision. We train up to $E_{\max} = 50$ epochs with early stopping ($P = 5$) on validation loss and report the checkpoint with the best F1@50. In inference, we use repetition collapsing and an optional median filter with $W = 3$.

D. Comparison with other methods

The results reported in Table IV compare RoboSubtaskNet with the MS-TCN and MS-TCN++ approaches on GTEA, Breakfast, and RoboSubtask datasets. In GTEA, RoboSubtaskNet outperforms both baselines in boundary-sensitive metrics (F1 @ 10, 25, 50 = 91.9, 89.6, 79.5 vs. 88.8, 85.7, 76.0 for MS-TCN++; Edit = 88.6 vs. 83.5), with comparable frame accuracy (78.9 vs. 80.1). In Breakfast, which features longer-horizon activities, our method trails MS-TCN++ across metrics (F1@50 = 30.4 vs. 45.9), reflecting the trade-off of a denser short-horizon dilation schedule. In the RoboSubtask dataset, where the labels are aligned with the manipulator primitives, RoboSubtaskNet achieves the best scores in all metrics (F1@50 = 94.2, Edit = 95.6, Accuracy = 92.15), indicating a strong suitability for robot-executable sub-tasks.

In summary, *RoboSubtaskNet* achieves the best boundary-sensitive metrics on *GTEA* and the best overall scores on *RoboSubtask*, while *MS-TCN++* remains stronger on *Breakfast*, consistent with its long-horizon focus.

TABLE IV: Comparison with state-of-the-art approaches on GTEA, Breakfast, and the RoboSubtask datasets

GTEA					
Model	F1@{10,25,50}			Edit	Acc
MS-TCN	85.8	83.4	69.8	79.0	76.3
MS-TCN++	88.8	85.7	76.0	83.5	80.1
RoboSubtaskNet	91.9	89.6	79.5	88.6	78.9
Breakfast					
Model	F1@{10,25,50}			Edit	Acc
MS-TCN	52.6	48.1	37.9	61.7	66.3
MS-TCN++	64.1	58.6	45.9	65.6	67.6
RoboSubtaskNet	48.4	41.7	30.4	52.03	53.5
RoboSubtask					
Model	F1@{10,25,50}			Edit	Acc
MS-TCN	91.5	91.4	91.0	91.8	89.2
MS-TCN++	92.6	92.4	92.2	93.9	91.0
RoboSubtaskNet	94.6	94.6	94.2	95.6	92.15

E. Ablations and qualitative analysis

Table V summarizes experiments that isolate the effect of different loss combinations on the RoboSubtask dataset. Using only the cross-entropy loss yields reasonable baseline performance. Augmenting cross-entropy with the temporal smoothing term (T-MSE) produces a small improvement in the Edit score from 64.2 to 64.6. In contrast, adding the transition-aware loss together with T-MSE yields large

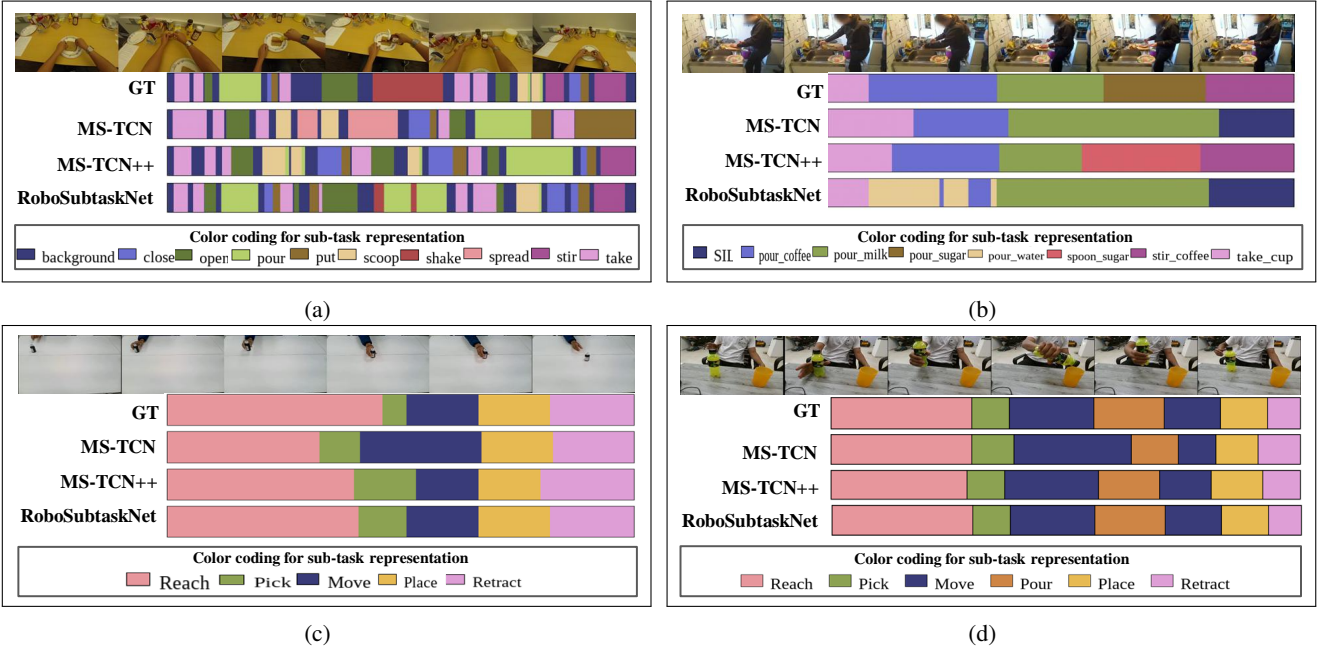


Fig. 5: Qualitative results of RoboSubtaskNet with MS-TCN and MS-TCN++ approaches. One example video is shown from each dataset: (a) GTEA and (b) Breakfast. Two examples (c), (d) from RoboSubtask for *pick and place* and *pick and pour* tasks, respectively. For each example, the video collage is presented along with the ground truth and predicted segmentation.

TABLE V: Comparison of different loss functions on the RoboSubtask dataset with the proposed approach

Loss	F1@{10, 25, 50}			Edit	Acc
L_{CE}	92.3	91.9	90.1	90.4	89.8
$L_{CE} + \lambda L_{T\text{-MSE}}$	92.9	92.0	91.5	91.5	90.6
$L_{CE} + \lambda L_{T\text{-MSE}} + \gamma L_{Trans}$	94.6	94.6	94.2	95.6	92.15

improvements across all metrics: F1@50 increases from 60.7 to 98.0, Edit increases from 64.2 to 98.5, and frame accuracy increases from 79.9 to 96.2. These results indicate that explicitly penalizing rapid probability changes and implausible label switches is especially important for accurate segmentation of short-horizon, robot-executable sub-tasks.

Figure 5 presents qualitative results: one video from each GTEA and Breakfast, and two videos from RoboSubtask (pick and place and pick and pour). For each example, we display the video collage, ground-truth segmentation, and predictions from MS-TCN, MS-TCN++, and RoboSubtaskNet. On GTEA and RoboSubtask, RoboSubtaskNet produces cleaner boundaries and fewer over-segmentation artifacts than the baselines, particularly around brief transitions such as reach to pick and place to retract. In Breakfast, which contains long-horizon composite activities, RoboSubtaskNet remains competitive with MS-TCN but occasionally under-segments extended activities, consistent with the method’s design emphasis on dense local coverage. These qualitative and quantitative outcomes can be attributed to the combination of attention-based fusion which balances RGB and flow cues, the Fibonacci dilation schedule which provides denser short-horizon temporal coverage, and the transition-aware loss which suppresses implausible label switches, together

yielding robust sub-task segmentation for robot-executable demonstrations.

F. Real-world tasks evaluation

We evaluated the overall performance of our methodology on four representative manipulation tasks. Figure 4a illustrates the pick and place task, Figure 4b depicts the pick and pour task, Figure 4c shows the cleaning task of the work surface, and Figure 4d presents the pick and give task. Each figure demonstrates the robot’s ability to learn from human demonstrations, identify the individual sub-tasks performed in those demonstrations, and execute the appropriate sub-task sequence using the robot execution model.

1) *Task performance and execution analysis:* We evaluated the proposed system on four distinct manipulation tasks, conducting 20 tests for each. The results, summarized in Table VI, demonstrate the robustness of our approach. The system achieved 95% success rate for both table cleaning & pick and place tasks, and 90% for pick and pour task. The interactive pick and give task produced an 85% success rate.

An important aspect of our evaluation is the time needed for the prediction of sub-tasks from video demonstrations. In our experiments, the input videos ranged from 3 to 25 seconds (approximately 90 to 750 frames at 30 fps). Shorter inputs (3 seconds or 90 frames) required less than 10 – 15 seconds for sub-task prediction, while the longest inputs (25 seconds or 750 frames) took about 1 – 1.5 minutes. This scalability supports the feasibility of our method for real-time applications.

For physical execution, the robot completed the tasks in 30 to 60 seconds, with variations depending on the complexity and duration of the sub-tasks required for each task.

TABLE VI: Overall task-wise evaluation

Task	Successful runs	Failed runs	Success rate (%)	Sub-task prediction time (s)	Task execution time (s)
Pick & Pour	18	2	90	60–90	50–60
Table Cleaning	19	1	95	60–90	50–60
Pick & Give	17	3	85	60–90	30–40
Pick & Place	19	1	95	60–90	45–50

2) *Failure analysis*: In all 80 trials, our system achieved a 91.25% success rate. We analyze 7 failures in all these tasks. As detailed in Table VII, issues occurred at the execution level: 42.85% from the physical robot execution model; these failures were caused by perception errors such as object detection inaccuracy, motion singularities, and grasp slippage, the other 28.57% from general system failures (e.g., system lags, robot hangs). The remaining 28.57% of failures originated in the planning stage, caused by an incorrect prediction of sub-task sequence.

TABLE VII: Failure analysis (7 failures across all tasks)

Failure Cause	Failures	Percentage (%)
Robot execution model	3	42.85
Sub-task Sequence Prediction	2	28.57
System Failure	2	28.57

IV. CONCLUSION

We presented a multi-stage *human-to-robot sub-task segmentation* framework that couples attention-enhanced I3D features (RGB+Flow) with a modified MS-TCN using a Fibonacci dilation schedule and transition-aware regularization. To bridge vision benchmarks and robotic execution, we introduced RoboSubtask, a sub-task annotated dataset in healthcare and industrial settings, and validated end-to-end deployment on a 7-DoF Kinova Gen3 by deterministically mapping predicted sub-task labels to primitive parameters and executing the resulting sequence. The experiments further show strong segmentation performance on the datasets (GTEA, RoboSubtask) across segmental F1@{10, 25, 50} and Edit score, underscoring that the proposed perception stack improves both recognition quality and downstream robot reliability.

Our current system relies on supervised sub-task labels, short-horizon manipulation assumptions, and monocular RGB+flow sensing; mapping from labels to skills is deterministic and only lightly monitored at run-time. Future work will explore (i) self-supervised and active annotation strategies to scale sub-task labeling, (ii) tighter perception-control coupling via closed-loop policies with uncertainty and safety-aware planning, and (iii) longer-horizon task composition segmentation and failure recovery. We believe these directions will further strengthen the bridge from fine-grained video understanding to robust, deployable human–robot collaboration.

REFERENCES

- [1] J. Mišekis, P. Caroni, P. Duchamp, A. Gasser, R. Marko, N. Mišekienė, F. Zwilling, C. de Castelbajac, L. Eicher, M. Früh, and H. Früh, “Lio-a personal robot assistant for human–robot interaction and care applications,” *IEEE Robotics and Automation Letters*, vol. 5, no. 4, pp. 5339–5346, 2020.
- [2] S. Wang, B. Wang, G. Shen, and D. Wu, “Visual-privileged co-learning for industrial board-to-board connectors force-guided assembly task,” *IEEE Robotics and Automation Letters*, vol. 10, no. 10, pp. 10154–10161, 2025.
- [3] F. Han, X. Yang, C. Reardon, Y. Zhang, and H. Zhang, “Simultaneous feature and body-part learning for real-time robot awareness of human behaviors,” in *International Conference on Robotics and Automation (ICRA)*, p. 2621–2628, IEEE Press, 2017.
- [4] K. P. Hawkins, S. Bansal, N. N. Vo, and A. F. Bobick, “Anticipating human actions for collaboration in the presence of task and sensor uncertainty,” in *International conference on Robotics and automation (ICRA)*, pp. 2215–2222, IEEE, 2014.
- [5] C. Brooks, M. Atreya, and D. Szafrir, “Proactive robot assistants for freeform collaborative tasks through multimodal recognition of generic subtasks,” in *International Conference on Intelligent Robots and Systems (IROS)*, pp. 8567–8573, IEEE/RSJ, 2018.
- [6] A. Fishman, C. Paxton, W. Yang, D. Fox, B. Boots, and N. Ratliff, “Collaborative interaction models for optimized human–robot teamwork,” in *International Conference on Intelligent Robots and Systems (IROS)*, pp. 11221–11228, IEEE/RSJ, 2020.
- [7] E. Johns, “Coarse-to-fine imitation learning: Robot manipulation from a single demonstration,” in *International Conference on Robotics and Automation (ICRA)*, pp. 4613–4619, IEEE, 2021.
- [8] F. Semeraro, A. Griffiths, and A. Cangelosi, “Human–robot collaboration and machine learning: A systematic review of recent research,” *Robotics and Computer-Integrated Manufacturing*, vol. 79, p. 102432, 2023.
- [9] J. Thumm, F. Trost, and M. Althoff, “Human–robot gym: Benchmarking reinforcement learning in human–robot collaboration,” in *International Conference on Robotics and Automation (ICRA)*, pp. 7405–7411, IEEE, 2024.
- [10] A. Fathi, Y. Li, and J. M. Rehg, “Learning to recognize daily actions using gaze,” in *Proceedings of the European Conference on Computer Vision (ECCV)*, 2012.
- [11] H. Kuehne, A. Arslan, and T. Serre, “The language of actions: Recovering the syntax and semantics of goal-directed human activities,” in *Proceedings of the IEEE Conference on Computer Vision and Pattern Recognition (CVPR)*, 2014.
- [12] S. Stein and S. J. McKenna, “Recognising complex activities with histograms of relative tracklets,” *Computer Vision and Image Understanding (CVIU)*, 2016. 50Salads dataset.
- [13] Y. Abu Farha and J. Gall, “Ms-ten: Multi-stage temporal convolutional network for action segmentation,” in *Proceedings of the IEEE/CVF Conference on Computer Vision and Pattern Recognition (CVPR)*, 2019.
- [14] S. Li, Y. Abu Farha, A. Richard, and J. Gall, “Ms-tcn++: Multi-stage temporal convolutional network for action segmentation,” *IEEE Transactions on Pattern Analysis and Machine Intelligence (TPAMI)*, 2020.
- [15] F. Yi, H. Wen, and T. Jiang, “Asformer: Transformer for action segmentation,” in *Proceedings of the British Machine Vision Conference (BMVC)*, 2021.
- [16] L. Ding and C. Xu, “Weakly-supervised action segmentation with iterative soft boundary assignment,” in *Proceedings of the IEEE Conference on Computer Vision and Pattern Recognition (CVPR)*, 2018.
- [17] J. a. Carreira and A. Zisserman, “Quo vadis, action recognition? a new model and the kinetics dataset,” in *Proceedings of the IEEE Conference on Computer Vision and Pattern Recognition (CVPR)*, 2017.
- [18] J. Carreira and A. Zisserman, “Quo vadis, action recognition? a new model and the kinetics dataset,” in *Proceedings of the IEEE Conference on Computer Vision and Pattern Recognition (CVPR)*, pp. 6299–6308, 2017.
- [19] W. Kay, J. Carreira, K. Simonyan, and et al., “The kinetics human action video dataset,” *arXiv preprint arXiv:1705.06950*, 2017.
- [20] A. J. Ijspeert, J. Nakanishi, H. Hoffmann, P. Pastor, and S. Schaal, “Dynamical movement primitives: learning attractor models for motor behaviors,” *Neural computation*, vol. 25, no. 2, pp. 328–373, 2013.
- [21] K. Robotics, “Kinova gen3 ultra lightweight robot user guide,” 2020.